Stratospheric aerosols and C 6 H 6 in Jupiter's south polar region from JWST/MIRI observations

Pablo Rodríguez-Ovalle, Sandrine Guerlet, Thierry Fouchet, Jake Harkett, Thibault Cavalié, Vincent Hue, Sandrine Vinatier, Manuel López-Puertas, Leigh Fletcher, Emmanuel Lellouch, et al.

A&A, 691, A51 (2024)
https://doi.org/10.1051/0004-6361/202451453

Astronomy & Astrophysics

Stratospheric aerosols and C_6H_6 in Jupiter's south polar region from JWST/MIRI observations

Pablo Rodríguez-Ovalle[1,⋆], Sandrine Guerlet[2], Thierry Fouchet[1], Jake Harkett[3], Thibault Cavalié[4,1], Vincent Hue[5], Sandrine Vinatier[1], Manuel López-Puertas[6], Leigh N. Fletcher[3], Emmanuel Lellouch[1], Ricardo Hueso[7], Imke de Pater[8,9], Glenn S. Orton[10], Michael T. Roman[3], Heidi B. Hammel[11], Stefanie N. Milam[12], and Oliver R. T. King[3]

[1] LESIA, Observatoire de Paris, Université PSL, CNRS, Sorbonne Université, Université Paris-Cité, Meudon, France
[2] Laboratoire de Météorologie Dynamique/Institut Pierre-Simon Laplace (LMD/IPSL), Sorbonne Université, CNRS, École Polytechnique, Institut Polytechnique de Paris, École Normale Supérieure (ENS), PSL Research University, Paris, France
[3] School of Physics and Astronomy, University of Leicester, University Road, Leicester, LE1 7RH, UK
[4] Laboratoire d'Astrophysique de Bordeaux, Univ. Bordeaux, CNRS, B18N, allée Geoffroy Saint-Hilaire, Pessac 33615, France
[5] Aix-Marseille Université, CNRS, CNES, Institut Origines, LAM, Marseille, France
[6] Instituto de Astrofísica de Andalucía, Consejo Superior de Investigaciones Científicas (CSIC), Glorieta de la Astronomía s/n, 18008 Granada, Spain
[7] Escuela de Ingeniería de Bilbao, Universidad del País Vasco, UPV/EHU, Bilbao, Spain
[8] Department of Earth and Planetary Science, University of California, Berkeley, CA 94720, USA
[9] Department of Astronomy, University of California, Berkeley, CA 94720, USA
[10] Jet Propulsion Laboratory, California Institute of Technology, 4800 Oak Grove Drive, Pasadena, CA 91109, USA
[11] Association of Universities for Research in Astronomy, Washington, DC, 20004, USA
[12] NASA Goddard Space Flight Center, Astrochemistry Laboratory, Greenbelt MD 20771, USA

Received 11 July 2024 / Accepted 13 September 2024

ABSTRACT

Context. The polar atmosphere of Jupiter is significantly affected by auroral activity, which can induce both thermal and chemical differences compared to the rest of the atmosphere. In particular, auroral activity enhances the production of various hydrocarbons, including benzene. Benzene could be a potential precursor to the formation of the stratospheric hazes.
Aims. We investigated the spatial distribution of the benzene abundance across latitudes ranging from 50°S to 81°S and 17°S to 25°S. Additionally, we examined the chemical origin of polar aerosols and their latitudinal distribution.
Methods. We employed *James Webb* Space Telescope (JWST) Mid InfraRed Instrument (MIRI) observations to measure the benzene abundance based on its emission at 674 cm^{-1}. Additionally, we examined the spectral dependence of the aerosol opacity within the 680–760 and 1380–1500 cm^{-1} spectral ranges, and mapped their distribution from 80°S–50°S.
Results. At latitudes lower than 60°S, benzene is found to be up to ten times more abundant compared to lower latitudes. This enhancement of C_6H_6 is well mixed longitudinally and not particularly concentrated inside the auroral oval. Photochemical models predict a decrease in the abundance as we approach the mid latitudes, but fail at polar latitudes as they do not include ion-neutral chemistry. Moreover, we find that the southern polar atmosphere is enriched with aerosols at ∼10 mbar. The optical depth of the aerosols increases at latitudes poleward of ∼60°S, similar to the enhancement of C_6H_6. These aerosols have spectral features similar to the aerosols of Titan and Saturn, and the mass loading is of $\sim 1.2 \pm 0.2 \times 10^{-4}$ g cm^{-2}. Finally, we quantified the impact of these aerosols on the retrieved temperature structure, causing a decrease in the temperature at pressure levels deeper than 10 mbar.
Conclusions. We find that the auroral precipitation produces abundant stratospheric aerosols, which must play an important role in the chemistry and dynamics of the planet.

Key words. planets and satellites: atmospheres – planets and satellites: aurorae – planets and satellites: composition – planets and satellites: gaseous planets

1. Introduction

The influx of energetic charged particles into Jupiter's polar regions is driven by its prominent magnetosphere. This particle precipitation deposits energy in the upper atmosphere of the planet and, as a consequence, the polar region of Jupiter exhibits noticeable differences in comparison with the rest of the Jovian atmosphere. Among these, an increase in the stratospheric temperature, at pressure levels above 5–10 mbar, has been observed within the auroral regions (Flasar et al. 2004; Sinclair et al. 2023; Rodríguez-Ovalle et al. 2024). Furthermore, several studies have found variations in the abundance of several hydrocarbons in Jupiter's polar stratosphere (Sinclair et al. 2018, 2023; Rodríguez-Ovalle et al. 2024). These variations are attributed to the interactions between charged particles and CH_4 (and its radicals), which consequently lead to the formation of various hydrocarbons within the auroral region (Flasar et al. 2004; Sinclair et al. 2017). It is unclear whether all hydrocarbons are affected in the same way. Some studies indicate an increase in the auroral region in some species such as C_2H_2 and C_2H_4 (Sinclair et al. 2018). However, the behavior of C_2H_6

⋆ Corresponding author; pablo.ovalle@obspm.fr

appears more complex: some studies report a depletion in the polar regions (Sinclair et al. 2018), others do not observe any clear trend (Sinclair et al. 2023), while recent results for the south polar region (SPR) show an enhancement of C_2H_6 with latitude at 3 mbar, not correlated with the position of the auroral oval (Rodríguez-Ovalle et al. 2024). Benzene (C_6H_6) was first detected in Jupiter by Kim et al. (1985) using the Voyager 1 Infrared Spectrometer (IRIS), and it also exhibits an enrichment in the polar stratosphere. Giles et al. (2023), using Juno Ultraviolet Spectrograph (UVS), also suggest an enhancement of C_6H_6 both within the auroral ovals and at similar latitudes outside the ovals. Moreover, Koskinen et al. (2016) and more recently Brown et al. (2024) also found an enhancement of benzene in the polar regions of Saturn by analyzing Cassini Ultraviolet Imaging Spectrograph (UVIS) stellar occultations, probing a pressure level of ∼1 µbar. Moreover, Fletcher et al. (2023) also found an enhancement of C_6H_6 in the North Polar Region of Saturn using MIRI Medium Resolution Spectroscopy (MRS). On the theoretical side, a chemical model of the Jovian atmosphere (Wong et al. 2003) predicts an increase in the benzene production rate within the auroral regions. In this model, ionic reactions lead to the formation of short-lived hydrocarbons (mainly cyclic $C_6H_7^+$ and C_3H_3), which consequently lead to the formation of C_6H_6 and benzene-ring compounds.

Another polar feature likely related to C_6H_6 is the presence of stratospheric aerosols. These aerosols were first identified on Jupiter by Owen & Mason (1969), from images in strong methane bands, which suggested the presence of hazes at both poles of the planet. The dynamics and altitudes of these aerosols were studied using images in the methane band acquired by the Voyager spacecraft and the Hubble Space Telescope (HST) by Sanchez-Lavega et al. (1998) who concluded that the observed aerosols are located in the region through 0.5 to 100 mbar and that part of the morphology associated with the more contrasted edges of the hazes could be caused by atmospheric Rossby waves. The complex morphology of the aerosols was also studied in HST images in the UV (Vincent et al. 2000). Follow-up studies of the polar hazes based on HST and Cassini data have shown large-scale ovals dark in the UV (Tsubota et al. 2023; Barbara et al. 2024). More recently, Zhang et al. (2013), using Cassini Imaging Science Subsystem (ISS) observations, were able to study their optical properties in more detail. Recent JWST near-infrared (NIR) observations with NIRCam (Hueso et al. 2023) have also revealed a noticeable presence of enhanced aerosols in the polar regions of Jupiter (see their Figure 1, Filters F164N, F212N, F335M, and F360M in their paper).

Regarding the chemical origin of these hazes, it is thought that C_6H_6 ring compounds can lead to the formation of aerosols by nucleation. Wong et al. (2003) showed that the consequent formation of C_6H_6 ring compounds chains could be possible using C_2H_2 during this process. This scenario gained credibility with the reported enrichment of C_2H_2 in the auroral regions (Sinclair et al. 2018; Rodríguez-Ovalle et al. 2024). This process would lead to the formation of complex hydrocarbon nuclei, that is polycyclic aromatic hydrocarbon aerosols (PAHs), which, after growing in size by nuclei accretion, precipitate to higher pressure levels. The pressure levels where these PAHs could form are still uncertain. While Wong et al. (2003) placed the formation of these PAHs at the same pressure level where C_6H_6 ring compounds should be formed (∼0.01 mbar), Lebonnois (2005), based solely on photochemical reactions, proposed that the peak mass production rate is located at 1 mbar for aliphatic polymers and PAHs. However, Lebonnois (2005) claimed that his model predicts only 3% of the total measured column density of benzene at low-to-mid latitudes. This discrepancy suggests that there might be a meridional transport of benzene from the poles to the equator, and that the aerosols are deposited near 1 mbar at low-to-mid-latitudes.

Using Cassini Composite Infrared Spectrometer (CIRS) spectra acquired in limb-viewing geometry, Vinatier et al. (2012) and Guerlet et al. (2015) were able to characterize the spectral dependence in the mid-infrared of the optical depth of aerosol present in Titan and Saturn, respectively. They found that these aerosols exhibited characteristic emissions around 700, 750, 1400, and 1450 cm^{-1}, and that these frequencies were consistent with vibration bands of aliphatic and aromatic hydrocarbons (Socrates 2004).

These features have remained elusive for Jupiter until now (Nixon et al. 2010). Recently, *James Webb* Space Telescope (JWST) observations analyzed by Rodríguez-Ovalle et al. (2024) hinted at the possible presence of aerosols at polar latitudes. They could then be the responsible of a decrease in lower stratospheric (10 mbar) temperature poleward of 60°S, forming a cold polar vortex that was previously observed by Fletcher et al. (2016) and Bardet et al. (2024). Characterizing the optical properties of these aerosols on Jupiter is key to better quantify their radiative impact on the Jovian temperature structure, as discussed by Zhang et al. (2015) and Guerlet et al. (2020).

In this paper, we present the analysis of the MIRI/MRS observations of Jupiter's SPR and Great Red Spot (GRS) concerning polar aerosols and benzene abundance in the southern hemisphere. We also used NIRCam images for context on the aerosol spatial distribution. This paper builds upon the work conducted in Rodríguez-Ovalle et al. (2024), as the same dataset was used in both studies. We present the retrieved abundance map of C_6H_6 at high spatial resolution at the south pole, as well as the spectral characterization of the polar stratospheric aerosols of Jupiter, along with a detailed analysis of its meridional trend.

2. JWST observations

2.1. MIRI/MRS instrument

Wells et al. (2015) have described the MIRI/MRS spectrometer, its operation modes and performances in detail. This instrument targeted Jupiter's SPR as part of the Early Release Science ERS #1373 program on December 24, 2022, and the GRS as part of the Guaranteed Time Observation GTO #1246 program on August 15, 2022, in order to study tropical latitudes. From these observations, spectra from 2080 to 347.5 to cm^{-1} (5 to 27 µm) of Jupiter were obtained. MIRI/MRS is a spectrograph capable of using its four integral field units (IFUs) to obtain spectral and spatial information of the planet almost simultaneously. Each of the four IFUs probes a specific wavenumber range and has slightly different Fields Of View (FOV), angular and spectral resolution. These IFUs are named as Channels, numbered from 1 to 4. These channels are in turn divided into three sub-bands ("SHORT", "MEDIUM", and "LONG"). The spectral information of each sub-band is obtained simultaneously for the 4 channels. Thus, to sample the full spectral range of MIRI/MRS, three successive exposures are required, one for each sub-band. Therefore, each observation generates a total of 12 hyperspectral cubes (three cubes per channel). During the SPR observation, three different tiles of the SPR were obtained, each of them centered at the south pole and covering a specific longitude range. Each of these tiles were obtained using a 2-point dither pattern, in order to increase the spatial coverage of the observation. The MIRI/MRS total exposure time is divided in a given number

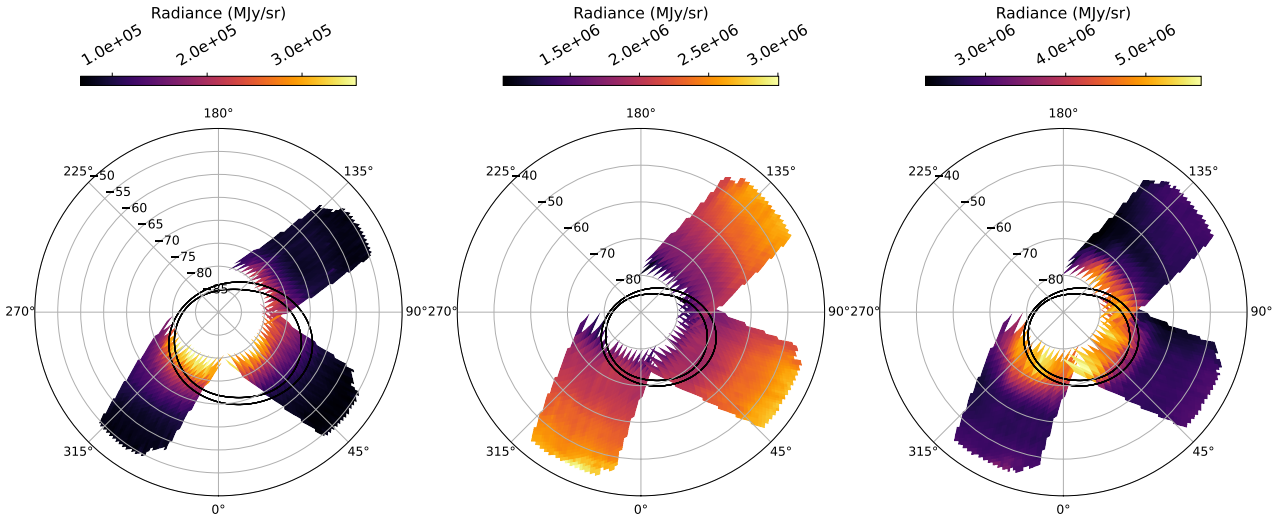

Fig. 1. Polar projections of the radiance measured by MIRI/MRS at 1450 cm^{-1} (left), 700 cm^{-1} (center) and 674 cm^{-1} (right). The black lines show the statistical position of the inner and outer limits of the auroral oval taken from Bonfond et al. (2017).

of integrations, each of them containing a specific number of groups. For our ERS #1373 observations, each sub-band was obtained with an exposure time of 527.258 s for a maximum of five groups per integration. For the GTO #1246 we only used the tile centered at 25°S, 300°W, with an exposure time of 433 s (eight integrations, four groups per integration). This dataset gave us access to latitudes closer to the equator, needed to better comprehend the global latitudinal variation of C_6H_6.

Fig. 1 shows the polar projection of the three tiles of our SPR observation. The three different SPR tiles were centered at 340°W, 70°W and 140°W (System III West). The left panel displays the radiance map for a CH_4 emission line at 1450 cm^{-1} (Channel 1-LONG), probing the mid-stratosphere (∼1–10 mbar). The central panel displays the radiance map for a wavenumber of 700 cm^{-1} (Channel 3-MEDIUM). This wavenumber corresponds to the continuum between the C_2H_2 ν_5 lines and probes the upper troposphere (∼100 mbar). Hence, the decrease in the radiance with latitude is due to a limb darkening effect. Finally, the right panel shows the radiance map for a wavenumber of 674 cm^{-1} (Channel 3-MEDIUM). At this wavenumber we find the C_6H_6 ν_{11} band. We observe that there exists an increase in the radiance not only within, but also outside the oval at high latitudes.

Due to the high radiance level of Jupiter and the high sensitivity of the JWST instruments, the observations were designed to be carried out in the FASTR mode. Specifically, in channels 3 and 4, Jupiter's luminosity overwhelms the instrument, leading to saturation when using more than two groups within the SPR and GRS datasets. Consequently, we were limited to use just one group to prevent saturation, and applied the desaturation method described in Rodríguez-Ovalle et al. (2024). We took advantage of MIRI being based on an up-the-ramp readout (Wells et al. 2015), a nondestructive readout method that allowed us to desaturate the spectra by reducing the number of groups included in the uncalibrated data. This method consequently reduces the quality of the spectra by reducing the signal to noise ratio (S/N), as we limited the access to a smaller number of groups to recover information that was previously lost by saturation. After modifying the uncalibrated files to avoid saturation, we used the version 1.11.3 of the MIRI reduction pipeline, and the CRDS (Calibration References Data System) file *jwst*_1119.*pmap* to obtain the hyperspectral cubes.

For this work, we have used the Channel 1-LONG for the aerosol feature located at 1450 cm^{-1}, and Channel 3-SHORT and MEDIUM for the aerosol features at 700 and 750 cm^{-1}, and for the C_6H_6 ν_{11} band (672–676 cm^{-1}). As the use of one group was required in Channel 3, we had to rescale the total radiance of the hyperspectral cubes by a correction factor of ∼1.025 for Channel 3-SHORT and 1.12 for Channel 3-MEDIUM. This factor was needed to reach radiance levels equal to those measured in the observation with five groups (four in the case of the GRS), for spectral regions that were not completely saturated. This factor is reasonably similar for all the spaxels of the hyperspectral cube, and approximately constant for all the wavenumbers of the sub-bands analyzed. This correction is similar to that performed in de Pater et al. (2023) for Io observations using JWST/NIRSpec. Unfortunately, even after applying the desaturation process, the C_2H_2 ν_5 Q-branch (720–740 cm^{-1}) still shows partial saturation, especially inside the auroral oval, and therefore has been omitted from our analysis.

The error estimation provided by the pipeline is too small to be credible. Generally, we found it necessary to scale the pipeline-generated error values by a factor ranging between 60 to 70. In the case of Channel 3, for which only one group was usable, this factor increases to 80. This factor has been obtained by quantifying the noise level observed in the continuum at 650 cm^{-1}. This ensures the error budget includes all the possible observational artifacts of MIRI/MRS (Rodríguez-Ovalle et al. 2024). This revised error assessment aligns well with the Root Mean Square error (RMSe) obtained when compared with the synthetic spectra, ensuring consistency in our analyses.

To analyze the aerosol spectral features, we have created mean latitudinal spectra with bins of 2-degree sampling step, and a width of 2.5 degrees, for latitudes between 51°S and 77°S, resulting in a total of 14 spectra. We limited our mean latitudinal spectra to the tile centered at 70°W, since the auroral oval is the most extended toward the equator, and best aligned with the MIRI/MRS FOV in this tile (see Fig. 1). This ensures that the averaged spectra sample exclusively either auroral or non-auroral regions (latitudes lower than 68°S). In contrast, if we were to utilize the tile centered at 340°W for generating the mean latitudinal spectra, the resulting mean spectrum at 71°S would average over both auroral and non-auroral individual spectra.

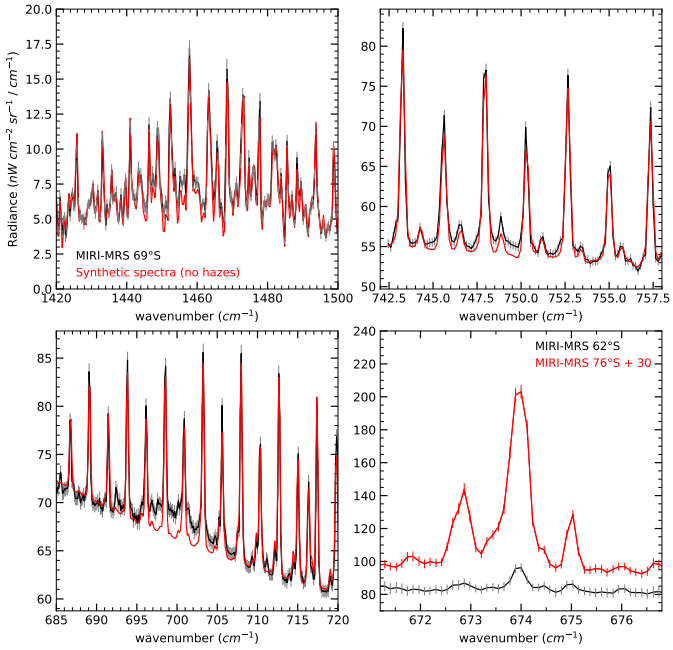

Fig. 2. Examples of the spectra used in this work. Top-Left: best fit of the CH_4 emission lines at 69°S with a model without stratospheric hazes (red line) compared to the observed spectra (black line), with an aerosol feature centered at 1450 cm^{-1}. Top-Right: best fit of the C_2H_2 emission lines with a model without stratospheric hazes (red line) compared to the observed spectra (black line), with an aerosol feature centered at 750 cm^{-1}. Bottom-Left: the same as in Top-Right but for the aerosol feature centered at 700 cm^{-1}. Bottom-Right: C_6H_6 ν_{11} spectra inside the auroral oval (red) and outside the auroral oval (black). The vertical lines show the error of the observations.

Figure 2 illustrates a representative selection of the spectra analyzed in this work. In the top-left, top-right, and bottom-left panels, we present a comparison between the observed spectra and the best-fit synthetic spectra generated without including aerosols, for the wavenumber ranges centered at 1450, 750, and 700 cm^{-1}, respectively. Notably, we observe that the synthetic spectra under-predict the observed radiances in these spectral regions, suggesting the presence of an additional opacity source. The fact that these features have higher radiances indicate that they would be located up in the stratosphere, where the temperatures are higher than the background temperature probed near the tropopause. In the bottom-right panel, we present a comparison between two C_6H_6 ν_{11} band spectra acquired at distinct latitudes (76°S in red and 62°S in black). The enhanced radiance therein is an effect of the elevated temperatures within the auroral oval, but also a potential enhancement of the C_6H_6 abundance. For determining the abundance of C_6H_6, we utilized all spaxels of the SPR dataset to create abundance polar maps and analyze its spatial distribution. For the GRS dataset, we used mean latitudinal spectra centered at 18°S, 22°S and 26°S.

2.2. NIRCam instrument

We have also utilized the NIRCam instrument in this study. NIRCam observed Jupiter for the first time on June 28, 2023, as part of the #1022 Engineering program. During this observation, several images were captured using the F323N filter, centered at 3096 cm^{-1} (3.23 μm). The images were processed with the version 1.11.3 of the pipeline, using the CRDS file *jwst_1119.pmap*. Due to Jupiter's low radiance at the spectral range of the F323N filter, desaturation processes were not required in this dataset. The molecules that dominate the emission in this spectral region are CH_4 with its ν_3 band, and H_3^+. While at low-to-mid latitudes, CH_4 dominates over H_3^+ in terms of emission, at latitudes closer to the poles, the H_3^+ emission is enhanced due to the auroral activity, becoming the main contributor of the radiance at high latitudes.

Figure 3 presents Jupiter as observed through the F323N NIRCam filter. The left panel displays a processed version of the F323N image using a combination of high pass-filters, with the brightness levels in a logarithmic scale. The right panel presents the same image with the contrast stretched to better highlight the underlying structures in the images, along with the levels of brightness in different locations of the planet. In the F323N filter, Jupiter shows a lack of structure at low-to-mid latitudes, due to the CH_4 probing higher pressure levels (~1 μbar), and a transition to the brightest regions in the two poles due to H_3^+ emissions.

3. Data analysis and results

For the analysis of the MIRI spectra, we have used a radiative transfer code that assumes an atmosphere in Local Thermodynamic Equilibrium (LTE) (Fouchet et al. 2016). This model contains spectroscopic information of the molecules present in the atmosphere of Jupiter at the spectral ranges analyzed: CH_4, C_2H_2, C_2H_6, NH_3 and C_6H_6 (Gordon et al. 2022). The forward modeling of the spectra requires prior assumptions regarding the vertical structure of the temperature and abundance of these species. We assumed the H_2 and He mole fractions of 0.862 and 0.137. For CH_4, we fixed the deep volume mixing ratio (VMR) at 1.90×10^{-3} consistent with the analysis of Niemann et al. (1996). We first used the CH_4 ν_4 band (1240 – 1330 cm^{-1}) to retrieve the stratospheric temperature between 20 and 0.01 mbar. As described in Rodríguez-Ovalle et al. (2024), several temperature retrievals were performed assuming different CH_4 homopause levels and the model that best fit each spectrum was selected as the baseline temperature profile. Then, we remapped the temperature retrieved from the CH_4 ν_4 band (channel 2-SHORT) to the corresponding grid for Channel 3-MEDIUM for the retrieval of C_6H_6 VMR. For this retrieval, additional information regarding the abundance of C_2H_2 is needed. This hydrocarbon features emission lines close to the C_6H_6 ν_{11} band and occupies the same spectral domain as the aerosol signatures centered at 700 and 750 cm^{-1}. Therefore, prior knowledge of C_2H_2 is needed for inferring information on the aerosol optical depth and the C_6H_6 abundance. We conducted a retrieval of C_2H_2 VMR using its ν_5 spectral range (685–750 cm^{-1}) excluding the spectral regions affected by the aerosols. Each spectrum was analyzed using an a priori C_2H_2 VMR profile corresponding to the homopause altitude derived from the temperature retrieval. The abundance profiles corresponding to different homopause altitudes were obtained from the model developed by Moses & Poppe (2017).

Fig. 4 illustrates the latitudinal variation of the temperature (left) and C_2H_2 abundance (right) taken from Rodríguez-Ovalle et al. (2024). On the left panel, at high latitudes within the auroral oval, we observe a double-peak warming occurring at pressure levels of 1 and 0.01 mbar, while temperatures at 10 mbar decrease toward the pole. On the right panel, we present the latitudinal evolution of C_2H_2 based on the work from Rodríguez-Ovalle et al. (2024). The C_2H_2 ν_5 band used to retrieve the C_2H_2 abundance is sensitive to pressure levels of 7 and 0.1 mbar. The largest variation with latitude is observed at 0.1 mbar, where the abundance decreases from $1.5 \pm 0.1 \times 10^{-6}$

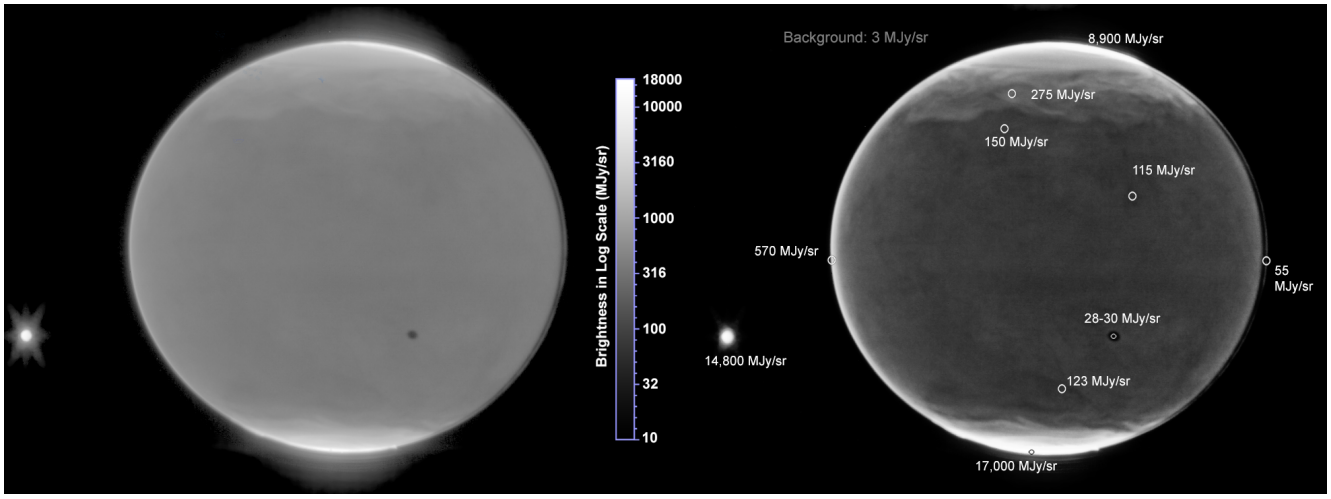

Fig. 3. Processed NIRCam images of Jupiter using the F323N filter. Left: Jupiter as seen through the NIRCam F323N filter on June 28, 2023, at 01:50:28 UTC, in log scale. Diffraction artifacts are observed near the bright auroral emissions. The bright satellite on the left side of the image is Europa, and its dark shadow over the planet shows weak atmospheric emissions not explainable by diffraction effects from the rest of the planet. Night-side limb emissions detached from the planet are observed in the west side of the planet (Sromovsky et al. 2022). Right: same as the left panel, but after enhancing the contrast. The circles mark the level of brightness of different regions.

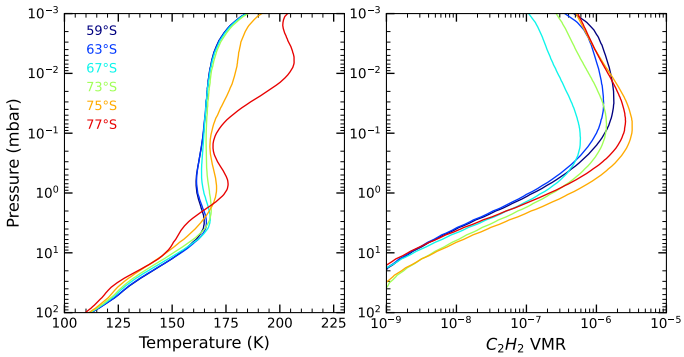

Fig. 4. Vertical profiles from Rodríguez-Ovalle et al. (2024). Left: mean latitudinal temperature profiles for certain polar latitudes. The temperature profiles have been derived between 100 and 0.01 mbar. Right: mean latitudinal C_2H_2 abundance profiles for the same latitudes. The abundance profiles have two degrees of freedom peaking at 5 and 0.1 mbar and have been retrieved using different a priori profiles, depending on the homopause location.

at 55°S to a minimum of $7\pm0.8\times10^{-7}$ at 63°S. At latitudes poleward of 63°S, the abundance experiences an enhancement due to auroral processes, with a peak value of 6×10^{-6} at 75°S.

These vertical profiles have been used as ancillary information in our radiative transfer calculations. The forward model is coupled to a Bayesian inversion method, already detailed in Guerlet et al. (2009), Fouchet et al. (2016) and Rodríguez-Ovalle et al. (2024). This inversion method generates a posterior profile from the difference between the observations and synthetic spectra generated with the a priori profile, until a best fit of the observed spectra is obtained. For this work, the retrieved quantities are the C_6H_6 VMR vertical profile, and the aerosol vertical profile.

The derived vertical profile will smoothly depart from its prior profile at the pressure levels where the contribution functions indicate spectral sensitivity. The new vertical profile is smoothed using a covariance matrix S, defined as a Gaussian with a specific Half-Width at Half-Maximum (HWHM). This HWHM is set to three scale heights to avoid unrealistic shapes on the retrieved vertical profiles. The inversion method will then generate new vertical profiles until a convergence criterion is reached, based on the goodness of the fit ($\chi^2 = \sum\left(\frac{\Delta I_i}{E_i}\right)^2$, where ΔI_i is the difference the radiance of the observed and the modeled spectrum for a specific wavenumber i, and E_i is the error associated with this radiance). The optimal vertical profile is selected when the change in χ^2 is less than 1% compared to the previous iteration. With this approach, we mitigate the uncertainties that arise from the ill-posed nature of the nadir remote sensing problem.

3.1. Retrieval of the C_6H_6 abundance

Prior to the retrieval of the abundance of C_6H_6, we performed a sensitivity analysis to characterize the pressure level probed by the ν_{11} band. In order to do that, we have analyzed the contribution functions for this spectral band. The kernel matrix shows no significant variation of the information content as a function of temperature, emission line contrast or emission angle, and the main information always remains located at ~0.5 mbar when using the a priori profile from Moses & Poppe (2017), which itself features a maximum abundance at ~0.5 mbar.

As the vertical profile of C_6H_6 remains largely unknown, we have explored alternative a priori profiles. As the C_6H_6 ν_{11} band information content is mainly sensitive to the location of its peak of abundance, we have studied the possibility that it could actually be probing deeper pressure levels of the atmosphere. For that, we have shifted the maximum value of abundance to deeper and higher pressure levels in the vertical profile (over a decade) from Moses & Poppe (2017) reference profile. We have then generated three a priori profiles: model A, peaking at 5 mbar, model B, peaking at 0.5 mbar (nominal profile from Moses & Poppe 2017), and model C peaking at 0.05 mbar. We have repeated our retrieval using each of these a priori profiles. As in the previous case, the information content does not vary with emission angle, or temperature structure, meaning that the weighting function seems to be mainly driven by the derivative of the abundance profile. Fig. 5 shows the retrieved abundance

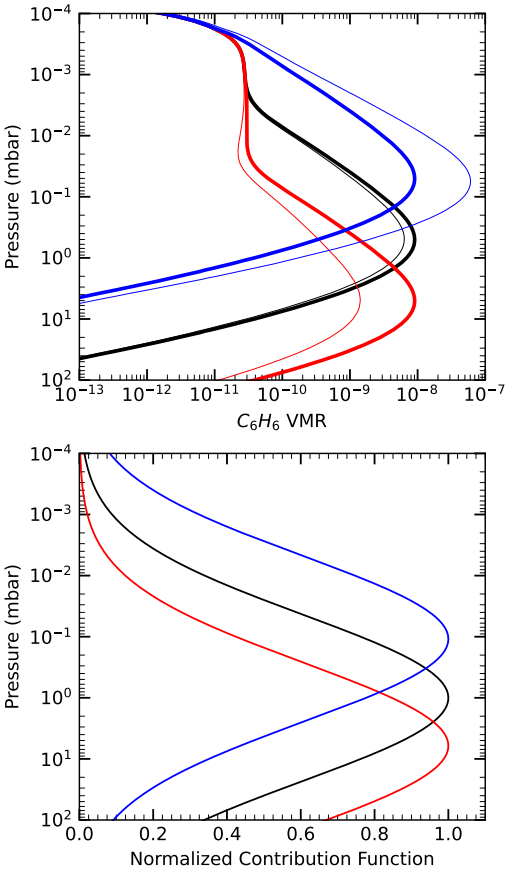

Fig. 5. Top: retrieved C_6H_6 vertical profile (red thin) using model A as a priori information (red thick), using model B as a priori information (black thick), and using model C as a priori information (blue thick), for the spectrum of Figure 6 (70°S, 69°W). Bottom: contribution functions for model A (red), model B (black) and model C (blue).

of benzene by using the three a priori profiles, for a spectrum located at 70°S, 69°W, together with their corresponding contribution functions.

The best-fit spectra obtained with the three different vertical profiles are indistinguishable from each other, demonstrating that we have no information about the vertical distribution of C_6H_6, and we are not able to retrieve a unique solution for this ill-posed problem. Fig. 6 compares the best-fit synthetic spectrum obtained with model B with the observations of the C_6H_6 emission line at 674 cm^{-1} (70°S, 69°W).

We can observe that our model is able to reproduce the benzene ν_{11} band located at 674 cm^{-1} and the C_2H_2 line at 675 cm^{-1}. In this spectral range, where our model only included spectroscopic information of the C_2H_2 ν_5 band and C_6H_6 ν_{11} band (Gordon et al. 2022), does not reproduce some observed spectral features. Indeed, we detect the C_6H_6 ν_{11}+ν_{16}-ν_{16} band at 672.876 cm^{-1} as well as a possible detection of the ν_{11}+ν_6-ν_6 band at 673.509 cm^{-1}, and of the isotope $^{13}C^{12}C_5H_6$ at 673.609 cm^{-1} (Hollenstein et al. 2006) in the observed spectrum. However, this is not a clear confirmation due to the magnitude of the error bars and the ripples affecting these spectral regions in MIRI/MRS (Fletcher et al. 2023). Unfortunately, we lack the spectroscopic information necessary to analyze these bands. The outcomes of our retrieval are presented in Fig. 7, showing a comparative analysis between the spatial distribution of C_6H_6 using model B and the polar structure observed in NIRCam F323N (from the #1022 commissioning program).

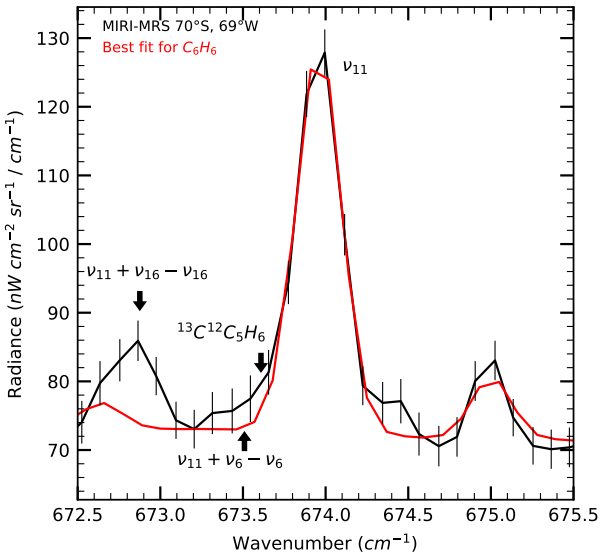

Fig. 6. Observed spectrum at 70°S, 69°W in black, and the modeled spectra for C_6H_6 for model A in red. Fits with other benzene a priori profiles are indistinguishable to the red one.

This retrieved spatial distribution remains consistent regardless of the vertical profile used as a priori, but with different abundance values. Fig. 8 shows the meridional trend of C_6H_6 retrieved at pressure levels of 5, 0.5 and 0.05 mbar (models A, B and C). It can be clearly seen that for all a priori profiles, we retrieve an enhancement in the C_6H_6 abundance in the SPR (poleward of 60°S), with a peak value of 5.5×10^{-9} when using model B. The maximum abundance is reached at 75°S and then presents a plateau up to 80°S. At lower latitudes, the meridional profiles decrease to reach a minimum located at ~50°S of 3.5×10^{-10} (model B), and then increase toward the GRS (17°S-25°S) where the abundance levels at 1.5×10^{-9} for model B.

The polar projections of the retrieved column densities (calculated for pressure levels between 100 mbar and 1μbar) are presented in the Appendix A. The values poleward of 67°S have a mean value of $2.5\pm0.2\times10^{15}$ molec cm^{-2} for model A, $1.5\pm0.3\times10^{15}$ molec cm^{-2} for model B and $8.5\pm0.6\times10^{14}$ molec cm^{-2} for model C. Equatorward of 57°S, they reach a mean value of $3\pm0.4\times10^{14}$, $2\pm0.2\times10^{14}$ and $1.7\pm0.2\times10^{14}$ molec cm^{-2} for models A, B and C, respectively. In the GRS, our analysis yielded column densities of $6\pm0.5\times10^{14}$, $3.5\pm0.4\times10^{14}$ and $2\pm0.3\times10^{14}$ molecules cm^{-2} when using models A, B and C, respectively.

We note that, while at latitudes equatorward of 65°S, the ratio between the column densities retrieved from different models is minimal (a factor of 1.8 between models A and B), at latitudes poleward of 65°S this ratio increases significantly, reaching a value of ~5 between models A and B. This variation is a consequence of different latitudinal temperature profiles at the peak pressures of the three a priori profiles. In model A, the bulk of C_6H_6 resides at 5 mbar, and at that altitude, the temperature slightly decreases toward the pole due to the effect of stratospheric aerosols. However, in models B and C, where the bulk resides at 0.5 and 0.05 mbar, the temperature increases toward the pole at those pressure levels, due to the auroral heating of the stratosphere. This leads to higher contributions of the temperature term in the radiance (the Planck function) in the polar region, and hence, it requires lower values of the column density to reach the observed radiance. For example, at 55°S, the

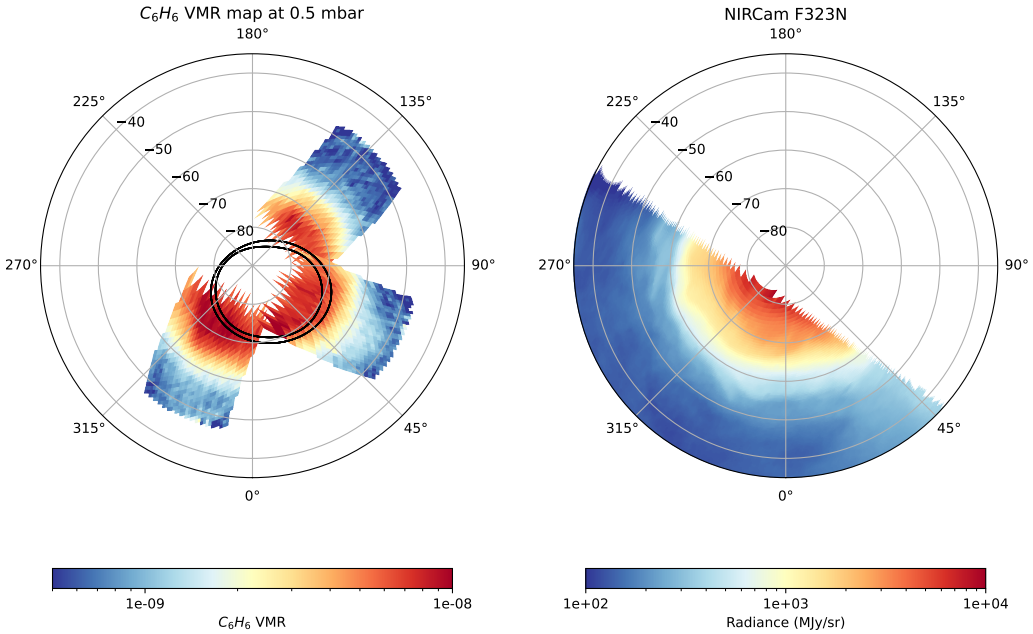

Fig. 7. Left: polar projection of the C_6H_6 abundance located at 0.5 mbar retrieved from model B. The black lines mark the statistical position for the southern auroral oval from Bonfond et al. (2017). Right: polar projection of a NIRCam image taken with the filter 323N on July 2022 as part of the #1022 commissioning program.

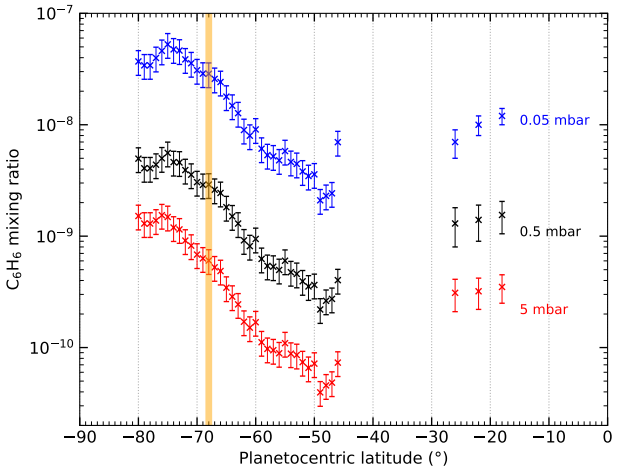

Fig. 8. Meridional trend of C_6H_6 at three pressure levels, corresponding to the three different a priori profiles: 5 mbar in red, 0.5 mbar in black, and 0.05 mbar in blue. The most equatorward latitude of the outer auroral oval is marked as an orange line (Bonfond et al. 2017). The values of the GRS dataset correspond to the latitudes 18°S, 22°S and 26°S.

temperature at 5 mbar was of 165 K, while at 0.5 mbar it was of 160 K, which implies a difference of 1.75 between the Planck functions calculated for a wavenumber at 674 cm^{-1}. Moreover, at 75°S, where the temperature at 5 mbar was 160 K and at 0.5 mbar was 175 K, this difference rises up to a factor of ~5.5.

3.2. Aerosol vertical distribution

The retrieval of the aerosol optical depth remains complex, as the information content for the hazes does not provide a specific pressure level where the aerosols could be present. This consequently leads to the retrieval of an unrealistic haze deck extending from 0.1 µbar to 100 mbar. Thus, we incorporate a mask feature into our model that restricts the inversion of the aerosol layer at the desired pressure levels. We have opted to invert an aerosol haze layer at a pressure level of ~2 mbar (model A*), and another at a pressure level of ~20 mbar (model B*). model A* is consistent with Guerlet et al. (2015) detection of Saturn's polar aerosols and Lebonnois (2005) models of aerosol production at Jupiter's equator. model B* aligns with the results from previous analysis of the Cassini/CIRS flyby of Jupiter (Zhang et al. 2013, 2015). The two model pressure levels (2 and 20 mbar) lie within the prediction presented in Wong et al. (2003), which reports that aerosols should be present at pressure levels between 1 and 100 mbar.

Fig. 9 compares the retrieved optical depth using the two a priori profiles (A* and B*) for the same spectrum located at 69°S (see Appendix B for model B*). The retrieved optical depth using model B* is higher by a factor of ~1.5, because the lower temperatures at 20 mbar than at 2 mbar require a larger aerosol optical depth to accurately reproduce the observed radiance.

3.3. Retrieval of the opacity's spectral dependence of the stratospheric aerosols

After investigating the variability of optical depth with different models, we conducted a comprehensive spectral analysis for all the spectra. Following the methodology employed in previous studies such as Vinatier et al. (2012) and Guerlet et al. (2015), we studied the spectral dependence of the aerosol signatures at 1450, 750, and 700 cm^{-1}. Each of the 14 latitudinal spectra were subdivided into 5 cm^{-1} intervals for the 1450 cm^{-1} feature within the range of 1380–1500 cm^{-1}, and 1 cm^{-1} intervals for the 700 and 750 cm^{-1} features (ranging between 680–720 and 740–760 cm^{-1}, respectively). We recall that the C_2H_2 Q-branch was excluded due to complete detector saturation. Using mean latitudinal temperature profiles and C_2H_2 abundance profiles as input data, we retrieved the aerosol optical depth for each interval. Given the narrow spectral ranges, we treated the aerosol opacity as gray hazes/aerosols, assuming identical spectral dependence within the analyzed wavenumber range. This approach enabled

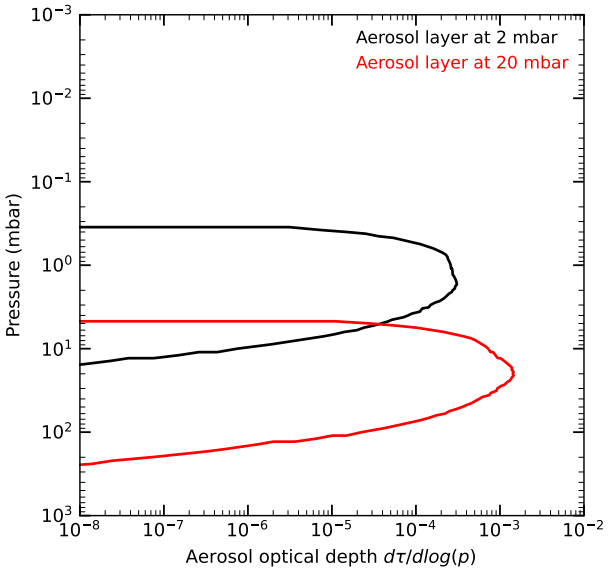

Fig. 9. Retrieved aerosol optical depth profile at 69°S for the spectral interval from 700 to 701 cm^{-1}. In the black profile we assumed model A* (2 mbar) and in the red one we assumed model B* (20 mbar).

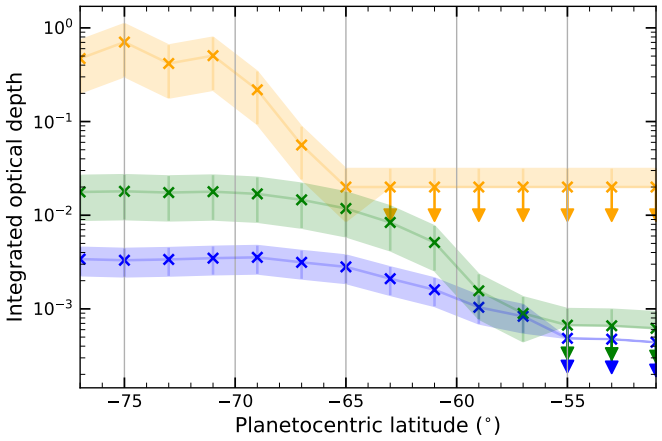

Fig. 10. Integrated optical depth over latitude retrieved from model B* for the features located at 700 cm^{-1} (blue curve), 750 cm^{-1} (green), and 1455 cm^{-1} (orange). The colored area shows the confidence interval of our measurements. The arrows mark the upper limit for the latitudes where the aerosol feature was no longer present.

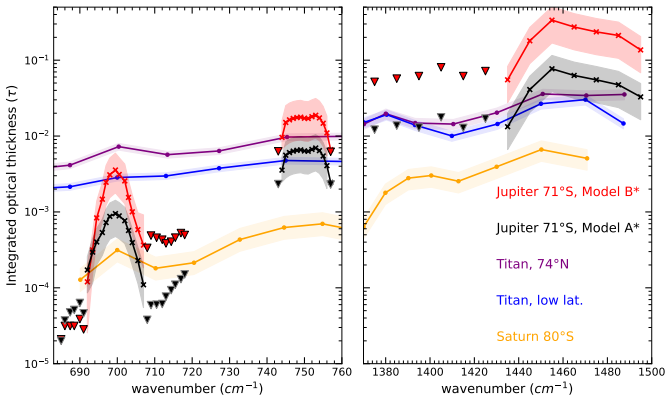

Fig. 11. Spectral dependence of the integrated optical depth from 0.4 to 70 mbar for a mean spectrum located at 71°S using model B* (red) and model A* (black), compared to the data from Vinatier et al. (2012) for Titan (integrated between 1.7 and 0.7 mbar) and Guerlet et al. (2015) for Saturn (integrated between 3 and 0.1 mbar) from Cassini/CIRS observations. The shaded areas show the magnitude of the error in each measurement. The upper limits are displayed as triangles.

independent measurements of the optical depth with a resolution of 1 cm^{-1} (5 cm^{-1} for the 1450 cm^{-1} feature), ten times finer than that employed in Guerlet et al. (2015) and Vinatier et al. (2012). This process was repeated for each of the 14 mean latitudinal spectra spanning from 51°S to 77°S, allowing us to retrieve the optical depth trends as a function of latitude. A detailed comparison between the observed and synthetic spectra with and without aerosols is presented in Appendix B.

Fig. 10 illustrates the dependence of the retrieved optical depth with latitude for the three different spectral features, centered at 1450, 750 and 700 cm^{-1}, respectively using model B*. Regarding the features at 750 and 700 cm^{-1}, we observe that the integrated optical depth (τ) is approximately constant at latitudes poleward of 65°S, with a value of 3.5×10^{-3} and 2×10^{-2}, respectively. At latitudes closer to the equator, the optical depth decreases, being undetected at latitudes equatorward of 55°S, where an upper limit of $\sim5\times10^{-4}$ was retrieved. The optical depth decreases more rapidly for the feature at 750 cm^{-1} compared to the feature at 700 cm^{-1}. In contrast, at 1450 cm^{-1}, the aerosols appear to be more concentrated within the auroral oval, rapidly decreasing at latitudes equatorward of 70°S, with a maximum value at the pole of 0.5, and an upper limit at lower latitudes of 2×10^{-2}.

Figure 11 displays the spectral dependence of the integrated optical depth for the mean spectrum centered at 71°S. The exceptional sensitivity of MIRI/MRS observations enables us to discern three peaks of enhanced optical depth located at 1450, 750, and 700 cm^{-1}. Remarkably, these features align with the frequencies of stratospheric aerosols identified in Titan (Vinatier et al. 2012) and Saturn (Guerlet et al. 2015), suggesting a common origin for aerosol formation across these planetary bodies.

However, three significant comments should be made:

– Noticeable discrepancies exist in the integrated optical depth obtained from model A* and B*. Generally, the optical depth retrieved using model B* is approximately three times larger than that obtained using model A*. The validity of these models will be further discussed in Sect. 4.2.

– In both Titan and Saturn, an emission peak is observed between 1380 and 1400 cm^{-1}. This peak is absent in the JWST dataset, suggesting potential differences in the chemical composition of Jupiter's aerosols compared to Saturn and Titan.

– The spectral shape of the 700 cm^{-1} peak is sharper in Jupiter than the one observed in Saturn and Titan, with larger optical depth retrieved at the core and lower at the edges. This difference may stem from a probable degeneracy between tropospheric temperatures and aerosol optical depth. In the retrieval of C_2H_2 (680–760 cm^{-1}), the tropopause temperature ($\sim$100 mbar) was simultaneously derived. We had to perform a simultaneous inversion of the tropopause temperature ($\sim$100 mbar) as we did not have access to another spectral range sensitive to the temperature at these pressure levels due to saturation and oscillation artifacts in the spectra at wavenumbers smaller than 660 cm^{-1}. This was not the case of Guerlet et al. (2015), who had access to the 590–650 cm^{-1} spectral range. This process excluded

spectral regions containing evident aerosol features (690–710 cm^{-1}) and assumed no contribution from haze opacity outside this region. Indeed, retrieving simultaneously the temperature, the C_2H_2 abundance and the haze opacity is too ill-constrained from just nadir observations. The drawback is a small error on the retrieved tropospheric temperature that will map into an error on the retrieved haze opacity. This error has been estimated to ±0.3 K in the tropospheric temperature (based on the RMSe), and its propagation in terms of optical depth was included in the error bars of the figure. This is the reason why our retrieved optical depth error bars are larger than those expected solely on MIRI/MRS sensitivity. Hence, the integrated optical depth retrieved within the 680–690 and 710–720 cm^{-1} ranges should be treated as an upper limit (shown as triangles in the figure), as this opacity has minimal impact on the synthetic model (refer to Fig. B.1).

4. Discussion

4.1. Benzene chemistry

Our results indicate an increase in the abundance of C_6H_6 in the south polar region of Jupiter, from a minimum VMR of ~5×10^{-10} at 50°S to a maximum of ~5×10^{-9} poleward of 75°S when using model B with a peak at 0.5 mbar. The abundance enhancement is not restricted to the auroral oval. Rather, C_6H_6 is zonally homogeneous across the three tiles obtained in our observations. This spatial distribution closely resembles that of the stratospheric polar aerosols as imaged by NIRCam. A similar spatial distribution was previously qualitatively observed by Giles et al. (2023) (see their Fig. 5e), with a minimum around 60°S. Moving toward lower latitudes, their values seem to suggest a slight increase in their scaling factor, similar to the trend we observed (See Fig. 8).

Kim et al. (1985) were the first to report the detection of benzene in Jupiter's North Polar Region using Voyager IRIS spectroscopy, although they did not provide any estimates of its abundance. Bézard et al. (2001) could determine for the first time the abundance of benzene on Jupiter at lower latitudes. Their ISO-SWS spectra had a large field of view, encompassing latitudes from 45°S to 45°N. They retrieved the benzene column density using three different profiles mimicking that of other hydrocarbons: a C_2H_6-type profile yielding a column density of 1.3×10^{15} molecules cm^{-2}, a C_2H_2-type profile with a column density of 9×10^{14} molecules cm^{-2}, and a CH_3-type profile giving 1.5×10^{14} molecules cm^{-2}, with a ±20% uncertainty. Their C_2H_6 and C_2H_2-type profiles had the major contribution from the lower stratosphere, and are therefore closer to our model A, while their CH_3-type profile peaked in the shallower stratosphere and should be compared with our model C. The column densities inferred by Bézard et al. (2001) are smaller or similar to our maximum column densities measured at latitudes 67–75°S ($2.5\pm0.2\times10^{15}$ molecules cm^{-2} for our model A, and $8.5\pm0.6\times10^{14}$ for our model C), confirming the polar rise of the benzene abundance. In the GRS, our retrieved values ($6\pm0.5\times10^{14}$ molecules cm^{-2} and $2\pm0.3\times10^{14}$ for models A and C respectively) are slightly lower than that inferred by Bézard et al. (2001). This may suggest that the C_6H_6 abundance may further rise toward the equator, as predicted by photochemical models (Moses et al. 2007) for Saturn. However, such an interpretation remains to be confirmed by further JWST observations covering a larger latitudinal range.

The abundance of C_6H_6 could be determined by Sinclair et al. (2019) in their analysis of Voyager-IRIS and Cassini-CIRS datasets, in the North Polar Region. In their retrieval of the 1-mbar abundance of benzene, they scaled a C_6H_6 vertical profile assuming that it had the same vertical distribution as C_2H_2 (Moses et al. 2005). Our model B profile is the closest to their assumptions. Using this model B, we retrieve a C_6H_6 VMR of 3–4 ppbv at 0.5 mbar at polar latitudes, similar to the 2–3 ppbv reported by Sinclair et al. (2019). Our retrieved abundances reach a plateau in the polar region, with a mean value of ~5 ppbv poleward of 70°S. Additionally, the contrast with quiescent regions at 50°S is more pronounced in our analysis. While Sinclair et al. (2019) observed the largest VMR difference to be a factor of two between the polar regions and lower-latitude regions, that is, 50°S, our study reveals a contrast of about a factor of 10. Several studies have pinpointed a large temporal variability of the hydrocarbons chemistry in the Jovian polar regions (Sinclair et al. 2023; Rodríguez-Ovalle et al. 2024). For example, C_2H_2 and C_2H_6 can experience strong variations of their abundances due to solar wind compression affecting the Jovian magnetosphere (Sinclair et al. 2023). The small differences in the benzene abundance and in the contrast between auroral and non-auroral latitudes between our study or that of Sinclair et al. (2019) might be explained by such temporal variation as much as a different production yields between the North and south polar regions. Comparing our results with the theoretical models proposed by Wong et al. (2003), our retrieved abundances using model C (which is the most similar to the vertical profile used in their work) is only 1.5 times higher than that predicted by the model, showing a good agreement with the model.

As already studied for other planets with neutral photochemical models (Moses et al. 2007), the increase in C_6H_6 abundance in the polar regions requires a local source located close to the poles. These models predict a maximum of C_6H_6 production at the equator, and, since the chemical loss time of this species is much lower than the timescale of meridional transport, then just as for Saturn, benzene would be destroyed before it could reach and accumulate at the poles (Guerlet et al. 2015). Therefore, the most widely proposed hypothesis to explain the enrichment in C_6H_6 at the poles requires the addition of ionic chemical pathways triggered from auroral particle precipitations (Wong et al. 2000; Friedson et al. 2002; Wong et al. 2003).

The fact that our retrieved C_6H_6 is zonally homogeneous could imply that it predominantly resides at deeper pressure levels between 1 and 10 mbar. At these pressure levels, the auroral-related non-zonal jet detected by Cavalié et al. (2021) is thought to weaken (Rodríguez-Ovalle et al. 2024) and to allow longitudinal transport. Moreover, none of the maps of Figures 7 and A.1 show the influence of the enhanced homopause and hotspot at 0.01 mbar in the retrieved C_6H_6 column density, which should affect molecules at higher altitudes such as C_2H_2 and C_2H_4 (Rodríguez-Ovalle et al. 2024; Sinclair et al. 2019). This further suggests that the C_6H_6 detected in our study may reside at pressure levels deeper than 5 mbar. Hence it remains difficult to constrain the C_6H_6 vertical distribution in the polar regions from our results. We further note that fully confirming of the zonal distribution of C_6H_6 would require adding a fourth tile to our mosaic, centered at 225°W, but this was not possible within the confines of the ERS program. The mechanism that could prevent C_6H_6 to migrate to lower latitudes may be related to the presence of a cold polar vortex (Fletcher et al. 2016; Bardet et al. 2024) located in the upper troposphere and lower stratosphere, that extends toward latitudes of ~60° in both the northern and southern polar region of Jupiter.

Moreover, the hypothesis that C_6H_6 serves as a precursor for PAHs formation (Wong et al. 2000) is supported by the discovery

of aerosols at identical latitudes, as will be discussed in the following section.

4.2. Aerosol detection

4.2.1. Spatial distribution and chemical origin of the aerosols

Our study presents the first detection of aerosol spectral features in the mid-infrared spectral region, at 700, 750 and 1450 cm^{-1}, in Jupiter. These aerosols are located in the polar region, particularly at latitudes poleward of 60°S. The spectral features at 700 and 750 cm^{-1} are present at latitudes poleward of ~60°S, with a retrieved integrated optical depth of 3.5×10^{-3} and 2×10^{-2}, respectively when using model B*. For latitudes closer to the equator, we could only derive upper limits of 5×10^{-4} for the two spectral features at 700 and 750 cm^{-1}. The spectral signature at 1450 cm^{-1} is more confined to high latitudes than the other two, being present at latitudes poleward of 67°S, with a integrated optical depth of 0.5 when assuming model B*. The upper limit for latitudes closer to the equator for this feature is of 2×10^{-2}. This suggests that different aerosols coexist in the polar regions, one type carrying the 700 and 750-cm^{-1} features, and a second type the 1450-cm^{-1} signature.

Similar spectral features were previously observed by Cassini-CIRS in Titan (Vinatier et al. 2012) and Saturn (Guerlet et al. 2015). The high spectral resolution of MIRI/MRS enables us to differentiate between the broad aerosols contribution and the C_2H_2 lines, although a degeneracy between the aerosol optical depth and tropospheric temperatures still exists. This degeneracy limited our analysis accuracy in the wavenumbers where the aerosol signatures become stronger, only allowing for the determination of an upper limit in the spectral regions not affected by the aerosols. Our findings align with the scenario adopted for Saturn in Guerlet et al. (2015), supporting a connection between auroral energy deposition and aerosol production. Polar aerosols were also previously observed in the UV from HST observations (Vincent et al. 2000; Barbara et al. 2024) and more recently analyzed by Giles et al. (2021) from Juno-UVS observations, though their chemical origin remained elusive.

The spectral signatures at 750 and 700 cm^{-1} can predominantly originate from aromatic or aliphatic hydrocarbons. As predicted by Wong et al. (2000, 2003), C_6H_6 can facilitate the formation of PAHs through hydrogen abstraction and acetylene (which is also enhanced in the polar region). These signatures, as observed by Guerlet et al. (2015) and Vinatier et al. (2012), align with the scenario proposed by Wong et al. (2000), hosting vibration modes of mono-substituted benzene molecules such as phenyl-acetylene, a precursor to the formation of naphthalene (A_2), another known PAH. However, the C_6H_6 latitudinal distribution does not totally align with the latitudinal distribution of these aerosol features, which may indicate that the latter could arise from different precursors apart from aromatic hydrocarbons, such as other aliphatic hydrocarbons that are also enhanced in the auroral region, such as C_4H_2 and CH_3C_2H (Sinclair et al. 2019). These hydrocarbons could produce aliphatic hydrocarbons, as some emissions from out-of-plane bending and rocking vibration (Vinatier et al. 2012).

The feature observed at 1450 cm^{-1} was also observed in Titan and Saturn by Vinatier et al. (2012) and Guerlet et al. (2015). In these works, other features were present at 1380 and 1400 cm^{-1}, that are not present in our analysis. According to Vinatier et al. (2012), the feature at 1400 cm^{-1} could primarily stem from symmetrical C-H bending in CH_3 groups of the aliphatic chain. Moreover, aromatic hydrocarbons do not present any signature in this spectral region. The 1450 cm^{-1} feature in Jupiter is attributed preferably to the $>CH_2$ scissor vibration mode, as CH_3 groups would exhibit another feature around 1380 cm^{-1} (Socrates 2004), not detected in our JWST/MIRI dataset. However, we note that a C_3H_8 band which was not included in our spectroscopic dataset is also located at 1450 cm^{-1}, as was noted in Nixon et al. (2009). Hence, this could imply that the higher optical depth within the oval would correspond to an enhancement of C_3H_8 rather than an enhancement of the aerosol optical depth. Nevertheless, the residuals do not show any clear evidence of the shape of this C_3H_8 band (see Fig. B.1).

Then, regarding the chemical origin of the aerosols, the aerosols present at 1450 cm^{-1} would be due to aliphatic hydrocarbons, and be more concentrated at higher latitudes. The features at 700 and 750 cm^{-1} would be produced by aromatic hydrocarbons and would be more extended toward lower latitudes. If this is the case, aliphatic aerosols may be more concentrated within the oval. The possible coexistence of aliphatic and aromatic hydrocarbon aerosols within the auroral oval could then contribute to the formation of the dark aerosol UV oval observed at auroral regions (Barbara et al. 2024; Tsubota et al. 2023), potentially due to the higher UV absorption capacity of aliphatic hydrocarbons.

Moreover, the differences between the latitudinal distribution of the different features may also suggest that the three are actually probing the same aerosols at different pressure levels of the stratosphere. The feature at 1450 cm^{-1} could then be probing the aerosols at higher altitudes (~1 mbar) within the oval, where they could be being produced by ion-neutral chemistry in the upper stratosphere of the auroral region. The feature at 750 cm^{-1} would probe deeper in the atmosphere, at pressure levels where the auroral jet is no longer present, allowing the aerosols to escape from the auroral region. Finally, the feature at 700 cm^{-1} would probe similar pressure levels, with a similar spatial distribution than the aerosols at 750 cm^{-1} but with a smaller optical depth.

In the context of the integrated optical depth depicted in Fig. 11, the peaks at 1450, 750, and 700 cm^{-1} exhibit higher values compared to Saturn. Taking the retrieved optical depth from model B* as the reference profile (aligned with the theoretical aerosol deposition height estimated by Wong et al. (2003) and with the direct measurements of Zhang et al. 2013), the retrieved optical depth of these features are approximately ~10 times larger than in Saturn. This may reflect the fact that auroral energy deposition in Jupiter is roughly ten times higher than in Saturn, indicating a proportional enhancement in aerosol production on Jupiter as predicted by Guerlet et al. (2015).

Regarding the potential contribution of other aerosols on Jupiter's aerosol budget, Guerlet et al. (2015) dismissed the contribution of amine vibration modes (N-N and N-H) due to the very low nitrogen content in Saturn's atmosphere. Even in Titan's predominantly nitrogen atmosphere, Vinatier et al. (2012) identified that the most prominent features are caused by C-H bond vibrations. The sole amine vibration modes in the mid-infrared are centered at 1415 and 1427 cm^{-1} (Vinatier et al. 2012), with no corresponding signature found in our study. We remain cautious about detecting an aerosol feature possibly linked to amine vibration modes around 1410 cm^{-1} in Saturn by Guerlet et al. (2015), as Cassini-CIRS encountered aliasing issues in this spectral range. It is noteworthy that in Jupiter, HCN depletion (Cavalié et al. 2023) coincides precisely with the latitude where the optical depth of aerosols, as observed in our study and in Giles et al. (2021), starts to increase (around ~60°S). This observation suggests that polar aerosols could potentially

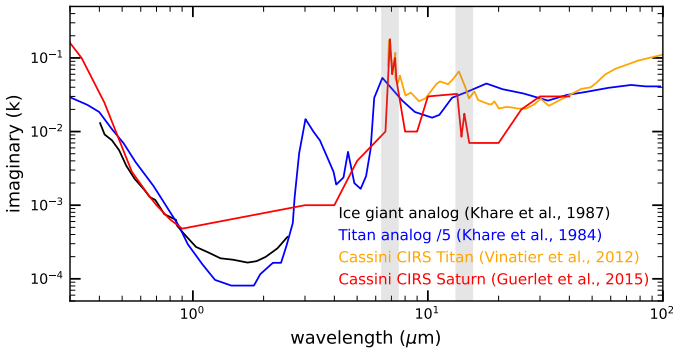

Fig. 12. Imaginary part (k) of the refractive index for the aerosols. Jupiter analog experiment (Khare et al. 1987) is shown in black, the tholin experiment (Khare et al. 1984) reduced by a factor of five is shown in blue, the Titan Cassini-CIRS observations (Vinatier et al. 2012) are shown in orange and the Saturn Cassini-CIRS observations (Guerlet et al. 2015) are shown in red. The gray regions mark the spectral region where the aerosols were analyzed in this work.

be a mixture of aromatic hydrocarbons and amine hydrocarbons, arising from a chemical process where HCN is transformed or destroyed to form these compounds.

4.2.2. Aerosol mass loading

Similarly to Guerlet et al. (2015), we have determined the aerosol partial column density. For that, we used:

$$\tau_{int,\lambda} = \pi r^2 Q_{ext,\lambda} N, \quad (1)$$

where $\tau_{int,\lambda}$ is the integrated optical depth between 70 and 0.4 mbar for a specific wavelength, r is the radii of the aerosol particles, $Q_{ext,\lambda}$ the extinction efficiency factor for a specific wavenumber, and N the aerosol column density.

We calculated the aerosol extinction coefficient Q_{ext} using a Mie-scattering code. For this, we needed previous assumptions on r and the real (n) and imaginary (k) parts of the refractive index at the specific wavenumber in the mid-infrared.

For n and k, we considered values from the tholin experiment aimed at simulating the Titanian atmosphere (Khare et al. 1984), adjusted by a factor of approximately five to align with the values obtained by Khare et al. (1987) for an ice giant analog. This adjustment factor ensures that the values of k in the near-infrared are also consistent with those used in Zhang et al. (2015). Additionally, we examined the values used in Guerlet et al. (2015) for Saturn from Cassini/CIRS observations.

Fig. 12 displays the different k index values for stratospheric aerosols. The values used by Guerlet et al. (2015) in the visible and near-infrared were themselves taken from the work of Karkoschka & Tomasko (2005) (based on imaging by HST). These values closely resemble those from the ice giant analog experiment and are consistent with the values employed by Zhang et al. (2015) in their study. Consequently, given the presumed similarity in aerosol properties between Saturn and Jupiter, we have adopted these values for calculating the mass loading in this work.

We have opted to test different scenarios for the aerosols. Apart from the residence pressure level, we have tested two possibilities for their size:

– Spherical aerosols (Fractal dimension 3): modeled with a mean radius of 0.1 μm, as Guerlet et al. (2015) described for Saturn.
– Fractal aggregates (Fractal dimension 2): modeled with a mean radius of 0.3 μm, as described in Zhang et al. (2013, 2015).

The size distributions were modeled as Gaussian distributions with a standard deviation σ of 0.05 μm.

For the spherical aerosol case, the mean spectrum location of 73°S, yields a column density of 4.0 ± 0.3 × 10^{10} particles cm^{-2} using model B* and 9.0 ± 0.6 × 10^{9} particles cm^{-2} using model A*. These values are ∼10 times higher than the column density observed for Saturn's aerosols (3.0 ± 0.8 × 10^{9} particles cm^{-2} from Guerlet et al. (2015)). Assuming a particle density of 1 g.cm^{-3} (as in Zhang et al. 2013), we calculated the total mass loading, resulting in 1.3 ± 0.2 × 10^{-4} g.cm^{-2} for model B* and 3.8 ± 0.4 × 10^{-5} g.cm^{-2} for model A*.

In the second case we assumed that the fractal aggregates would behave like equivalent spherical aerosols with a radius of 0.3 μm due to the diffraction effects in the mid-infrared, as the diffraction effects would prevent the differentiation between the inner monomers and the resulting agglomerate. We recalculated the values of Q_{ext} for this case and obtained column density of 2.5 ± 0.4 × 10^{8} particles cm^{-2} for model A* and 1.1 ± 0.2 × 10^{9} particles cm^{-2} for model B*. Consequently, the retrieved mass loading was 2.8 ± 0.5 × 10^{-5} g cm^{-2} for model A* and 1.2 ± 0.2 × 10^{-4} g cm^{-2} for model B*.

For the two sizes considered, the retrieved mass loading for an aerosol layer at 1 mbar (model A*) ranges from 2.3 × 10^{-5} g cm^{-2} to 4.2 × 10^{-5} g cm^{-2}. When assuming that the aerosol peak occurs at 20 mbar (model B*), the retrieved mass loading is approximately 1.25 × 10^{-4} g cm^{-2}. Zhang et al. (2013) attributed a total mass loading of about 10^{-4} g cm^{-2} for the polar stratospheric aerosols. This value is more consistent with the results for model B*. While a particle size of 0.3 μm was preferred for fitting the polar aerosols in the NIR (Zhang et al. 2013), we find that smaller sizes such as the 0.1 μm size retrieved for Saturn are also valid.

4.3. Impact of radiative properties of hazes on the retrieved temperature structure

In previous studies analyzing the CH_4 ν_4 band centered at 1306 cm^{-1} using the same JWST dataset (Rodríguez-Ovalle et al. 2024) presented a thermal field inverted without including any aerosol opacity. They observed a decrease in temperature at a pressure level of 10 mbar for latitudes poleward of approximately 60°S. This cold polar vortex has been observed for both poles of Jupiter using CIRS and ground-based data (Fletcher et al. 2016; Bardet et al. 2024). As the presence of an aerosol layer adds some opacity in Jupiter's polar stratosphere, the results of Rodríguez-Ovalle et al. (2024) need to be checked in this new context. To address this issue, we conducted a new temperature retrieval for mean latitudinal spectra using the aerosol spectral information presented in this study.

We generated aerosol models peaking at 1 and 20 mbar, assuming a gray optical depth in the range 1240–1330 cm^{-1} to retrieve the temperature. We used the optical depth retrieved for a latitude of 73°S between 1380 and 1400 cm^{-1} (the closest wavenumbers to the CH_4 ν_4 band). This value ranges between 0.01 and 0.05, depending on the assumed aerosol vertical profile. As indicated in Fig. 10, this aerosol opacity was assumed constant with latitude from 81°S toward 63°S, and then was assumed to decrease with latitude to become negligible equatorward of 59°S. We then performed the temperature retrieval as detailed in Rodríguez-Ovalle et al. (2024), but adding the aerosols opacity with the model A* and B* aerosol vertical profiles.

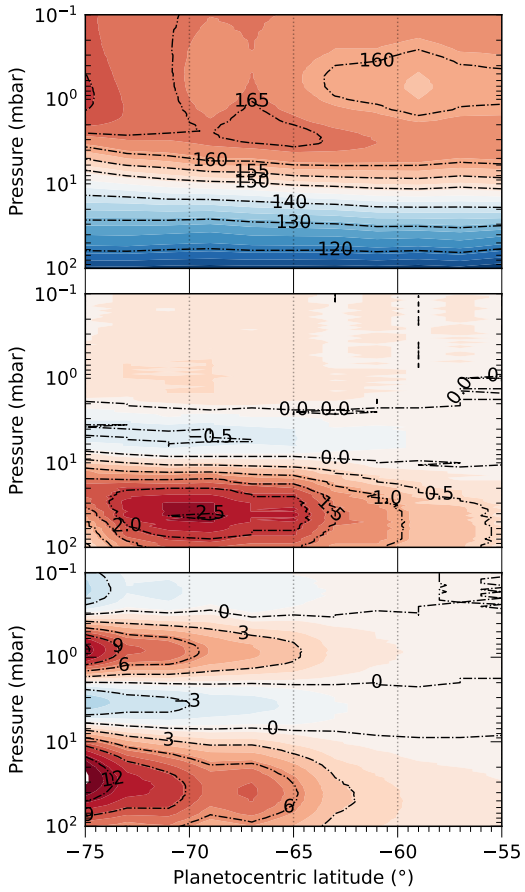

Fig. 13. Effects of the aerosols in the temperature retrieval. Top: latitude-pressure cross-sections of the retrieved temperature using the spectral range from 1240 to 1330 cm^{-1} without including aerosols in the radiative transfer model (Rodríguez-Ovalle et al. 2024). Center: Difference between the temperature profile without hazes and the temperature profile using a 20 mbar haze deck, that is model B* ($T_{aerosol=0} - T_{model-B*}$). Bottom: difference between the temperature profile without hazes and the temperature profile using a 2 mbar haze deck, that is model A* ($T_{aerosol=0} - T_{model-A*}$).

Figure 13 illustrates the difference in the meridional temperature structures retrieved without hazes, along with the temperature difference between this scenario and the scenario with aerosols from model A* (middle panel) and model B* (bottom panel).

Our analysis reveals that incorporating an aerosol layer at 1 or 20 mbar significantly modifies the retrieved temperature profile between 100 and 0.1 mbar. In both scenarios (model A* and model B*), introducing aerosols decreases the retrieved temperature at 20 mbar at latitudes poleward of 60°S, indicating the presence of a cold collar in Jupiter's south polar region, reinforcing the findings of Rodríguez-Ovalle et al. (2024). Moreover, we observed that adding aerosols at 1 mbar (model A*) adversely affects the spectral fit quality, suggesting that this approach may not be optimal. In contrast, the inclusion of aerosols at 20 mbar (model B*) yields χ^2 values that are as good as or better than those without aerosols, preserving the 1-mbar auroral hotspot detected in previous temperature analyses (Flasar et al. 2004; Sinclair et al. 2023) using not only the CH_4 ν_4 band but also the H_2 S(1) line at 600 cm^{-1}.

Our analyses suggest that the most suitable solution is the location of the aerosols around 20 mbar, aligning with previous studies Zhang et al. (2013, 2015). In model B*, the new retrieved temperature profiles exhibit a steeper temperature gradient with height, indicating higher static stability within this atmospheric region.

5. Conclusions

In this study, we utilized the MIRI/MRS instrument aboard JWST to investigate the south polar region of Jupiter (ERS 1373 dataset), as well as the Great Red Spot at low latitudes (GTO #1246, Harkett et al. 2022). For the south pole, three tiles were obtained on 24 December 2022. Each tile covered longitudes centered at 340°W, 70°W and 140°W, with the auroral oval visible in two of them. For the GRS, only one tile was analyzed, obtained on 15 August 2022, and centered at 300°W.

We focused on deriving and mapping the abundance of benzene across latitudes spanning from 17°S to 25°S and 45°S to 80°S. We found that C_6H_6 abundance has a maximum in the south polar region, and a minimum at 50°S. Its abundance seems to increase again toward the equator, as seen from the GRS dataset also analyzed in this work. The column densities retrieved between 100 mbar and 1 μbar from the GRS dataset are within the range proposed by Bézard et al. (2001) for mid-to-low latitudes. Interestingly, our findings challenge conventional photochemical models, which predict a decrease in benzene abundance toward the poles. Notably, benzene abundance is enhanced with a notable contrast of approximately 10-fold between auroral and quiescent regions. This suggests the need of including ion-neutral chemistry in the auroral region in order to produce the observed C_6H_6 enhancement. Moreover, the region exhibiting enhanced C_6H_6 levels aligns with the observation of aerosol features in the atmosphere, suggesting a potential link between the benzene enrichment and the aerosol presence in Jupiter's polar atmosphere.

Regarding the haze properties, we have estimated for the first time their optical depth in the thermal infrared, which will help to refine the computation of their radiative impact in atmospheric models (Zhang et al. 2015; Guerlet et al. 2020). Our analysis revealed distinctive spectral features at 700, 750, and 1450 cm^{-1}. These features, previously observed on Titan and Saturn (Vinatier et al. 2012; Guerlet et al. 2015), are indicative of aromatic and aliphatic hydrocarbons. The correlation between the high abundance of C_6H_6 and the abrupt appearance of these aerosols at polar latitudes supports the hypothesis put forth by Wong et al. (2000, 2003), that these aerosols originate from benzene, which can subsequently lead to the formation of polycyclic aromatic hydrocarbons (PAHs).

Furthermore, our analysis indicates that when assuming the aerosol layer located at 20 mbar (consistent with Zhang et al. 2013), we find an aerosol optical depth ten times larger than that observed in Saturn for these spectral features. This finding aligns with the notion that Jupiter experiences approximately ten times greater auroral energy input compared to Saturn, thereby enhancing haze production by such factor.

These hazes have a notable impact on the retrieved temperature structure of the polar region. Although the aerosol vertical distribution is not well constrained, its implementation in the temperature retrieval leads to significant cooler temperatures near 10 to 20 mbar, further enhancing the temperature latitudinal gradient previously observed in Rodríguez-Ovalle et al. (2024) and confirming the existence of a cold collar in Jupiter's polar region, characterized by a higher static stability. If the aerosol layer is assumed near 2 mbar, the independently established temperature hot spot at 1 mbar disappears and also the spectral fit is

worse. That suggests that the aerosols are located at higher pressures (near 20 mbar). Knowledge of the optical properties and residence levels of the aerosols are crucial to better constrain circulation patterns and the total stratospheric radiative budget, as both are sensitive to the aerosols properties (Guerlet et al. 2020).

We note that for a better determination of the longitudinal distribution of the aerosols and of C_6H_6, at least four MIRI tiles separated by about ~90 in longitude should be required. Future JWST observations of Jupiter should take this into account, and potential future observations of the North Polar Region could help to better assess the aerosol budget and benzene distribution in the two hemispheres.

Data availability

Level-3 calibrated Jupiter MIRI/MRS data from the standard pipeline are available directly from the MAST archive (https://mast.stsci.edu/portal/Mashup/Clients/Mast/Portal.html), MISSION: JWST, PROPOSAL-ID: 1373.

The radiative transfer and retrieval code used in this work and previous works (Fouchet et al. 2016; Guerlet et al. 2009) is available for download in Rodriguez-Ovalle (2024).

The JWST calibration pipeline is available via Bushouse et al. (2022), this work used version 1.11.3. The data products produced in this study (C_6H_6 and aerosol vertical profiles) are available from Rodriguez-Ovalle & Fouchet (2024).

Acknowledgements. This work is based on observations obtained with the NASA/ESA/CSA *James Webb* Space Telescope. The data were obtained from the Mikulski Archive for Space Telescopes at the Space Telescope Science Institute, which is operated by the Association of Universities for Research in Astronomy, Inc., under NASA contract NAS 5-03127 for JWST. These observations are associated with program #1373 (Observations 2, 4 and 26), which is led by co-PIs Imke de Pater and Thierry Fouchet. Data from JWST programs 1246 and 1247 were used for wavelength calibration. P.R.O. was supported by an Université Paris-Cité contract. T.C. acknowledges funding from CNES and from the Programme National de Planétologie. V.H. acknowledges support from the French government under the France 2030 investment plan, as part of the Initiative d'Excellence d'Aix-Marseille Université – A*MIDEX AMX-22-CPJ-04. M.L.P. acknowledges financial support from the Agencia Estatal de Investigación, MCIN/AEI/ 10.13039/ 501100011033, through grants PID2022-141216NB-I00 and CEX2021- 001131-S. I.d.P. is in part supported by the Space Telescope Science Institute grant JWST-ERS-01373. L.N.F., M.T.R. and O.T.R.K. were supported by STFC Consolidated Grant reference ST/W00089X/1. J.H. was supported by an STFC studentship. H.B.H. and S.N.M. acknowledge support from NASA JWST Interdisciplinary Scientist grant 21-SMDSS21-0013. R.H. was supported by grant PID 2019-109467GB-I00 funded by MCIN/AEI/ 10.13039/501100011033/ and was also supported by Grupos Gobierno Vasco IT1742-22. For the purpose of open access, the author has applied a Creative Commons Attribution (CC BY) licence to the Author Accepted Manuscript version arising from this submission. Some of this research was carried out at the Jet Propulsion Laboratory, California Institute of Technology, under a contract with the National Aeronautics and Space Administration (80NM0018D0004).

References

Barbara, J. M., West, R. A., Del Genio, A. D., & Sinclair, J. A. 2024, Icarus, 410, 115913
Bardet, D., Donnelly, P. T., Fletcher, L. N., et al. 2024, J. Geophys. Res. Planets, 129, e2023JE007902
Bézard, B., Drossart, P., Encrenaz, T., & Feuchtgruber, H. 2001, Icarus, 154, 492
Bonfond, B., Gladstone, G. R., Grodent, D., et al. 2017, Geophys. Res. Lett., 44, 4463
Brown, Z. L., Koskinen, T. T., Moses, J. I., & Guerlet, S. 2024, Icarus, 417, 116133
Bushouse, H., Eisenhamer, J., Dencheva, N., et al. 2022, https://doi.org/10.5281/zenodo.7038885
Cavalié, T., Benmahi, B., Hue, V., et al. 2021, A&A, 647, L8
Cavalié, T., Rezac, L., Moreno, R., et al. 2023, Nat. Astron., 7, 1048
de Pater, I., Lellouch, E., Strobel, D. F., et al. 2023, J. Geophys. Res. Planets, 128, e2023JE007872
Flasar, F. M., Kunde, V. G., Achterberg, R. K., et al. 2004, Nature, 427, 132
Fletcher, L. N., Greathouse, T. K., Orton, G. S., et al. 2016, Icarus, 278, 128
Fletcher, L. N., King, O. R. T., Harkett, J., et al. 2023, J. Geophys. Res. Planets, 128, e2023JE007924
Fouchet, T., Greathouse, T. K., Spiga, A., et al. 2016, Icarus, 277, 196
Friedson, A. J., Wong, A.-S., & Yung, Y. L. 2002, Icarus, 158, 389
Giles, R. S., Greathouse, T. K., Hue, V., et al. 2021, J. Geophys. Res. Planets, 126, e2021JE006928
Giles, R. S., Hue, V., Greathouse, T. K., et al. 2023, J. Geophys. Res. Planets, 128, e2022JE007610
Gordon, I. E., Rothman, L. S., Hargreaves, R. J., et al. 2022, J. Quant. Spectr. Rad. Transf., 277, 107949
Guerlet, S., Fouchet, T., Bézard, B., Simon-Miller, A. A., & Michael Flasar, F. 2009, Icarus, 203, 214
Guerlet, S., Fouchet, T., Vinatier, S., et al. 2015, A&A, 580, A89
Guerlet, S., Spiga, A., Delattre, H., & Fouchet, T. 2020, Icarus, 351, 113935
Harkett, J., Fletcher, L., Melin, H., et al. 2022, 16th Europlanet Science Congress 2022, online at https://www.epsc2022.eu/, EPSC2022-1006
Hollenstein, H., Piccirillo, S., Quack, M., & Snels, M. 2006, Mol. Phys., 71, 759
Hueso, R., Sánchez-Lavega, A., Fouchet, T., et al. 2023, Nat. Astron., 7, 1
Karkoschka, E., & Tomasko, M. 2005, Icarus, 179, 195
Khare, B. N., Sagan, C., Arakawa, E. T., et al. 1984, Icarus, 60, 127
Khare, B. N., Sagan, C., Thompson, W. R., Arakawa, E. T., & Votaw, P. 1987, J. Geophys. Res. Space Phys., 92, 15067
Kim, S. J., Caldwell, J., Rivolo, A. R., Wagener, R., & Orton, G. S. 1985, Icarus, 64, 233
Koskinen, T. T., Moses, J. I., West, R. A., Guerlet, S., & Jouchoux, A. 2016, Geophys. Res. Lett., 43, 7895
Lebonnois, S. 2005, Planet. Space Sci., 53, 486
Moses, J. I., & Poppe, A. R. 2017, Icarus, 297, 33
Moses, J. I., Fouchet, T., Bézard, B., et al. 2005, J. Geophys. Res. Planets, 110, E08001
Moses, J. I., Liang, M.-C., Yung, Y. L., & Shia, R.-L. 2007, Lunar Planet. Sci. Conf. 1338, 2196
Niemann, H. B., Atreya, S. K., Carignan, G. R., et al. 1996, Science, 272, 846
Nixon, C. A., Jennings, D. E., Flaud, J.-M., et al. 2009, Planet. Space Sci., 57, 1573
Nixon, C. A., Achterberg, R. K., Romani, P. N., et al. 2010, Planet. Space Sci., 58, 1667
Owen, T., & Mason, H. P. 1969, J. Atmos. Sci., 26, 870
Rodriguez-Ovalle, P. 2024, https://doi.org/10.5281/zenodo.11046342
Rodriguez-Ovalle, P., & Fouchet, T. 2024, https://doi.org/10.5281/zenodo.12704447
Rodríguez-Ovalle, P., Fouchet, T., Guerlet, S., et al. 2024, J. Geophys. Res. Planets, 129, e2024JE008299
Sanchez-Lavega, A., Hueso, R., & Acarreta, J. R. 1998, Geophys. Res. Lett., 25, 4043
Sinclair, J. A., Orton, G. S., Greathouse, T. K., et al. 2017, Icarus, 292, 182
Sinclair, J. A., Orton, G. S., Greathouse, T. K., et al. 2018, Icarus, 300, 305
Sinclair, J. A., Moses, J. I., Hue, V., et al. 2019, Icarus, 328, 176
Sinclair, J. A., Greathouse, T. K., Giles, R. S., et al. 2023, arXiv e-prints [arXiv:2304.08390]
Socrates, G. 2004, J. Raman Spectrosc., 35, 905
Sromovsky, L., de Pater, I., Fouchet, T., et al. 2022, AAS/Div. Planet. Sci. Meeting Abs., 54, 306.08
Tsubota, T., Wong, M., Stallard, T., Zhang, X., & Simon, A. 2023, Research Square, https://doi.org/10.21203/rs.3.rs-3370920/v1
Vinatier, S., Rannou, P., Anderson, C. M., et al. 2012, Icarus, 219, 5
Vincent, M. B., Clarke, J. T., Ballester, G. E., et al. 2000, Icarus, 143, 205
Wells, M., Pel, J.-W., Glasse, A., et al. 2015, PASP, 127, 646
Wong, A.-S., Lee, A. Y. T., Yung, Y. L., & Ajello, J. M. 2000, ApJ, 534, L215
Wong, A.-S., Yung, Y. L., & Friedson, A. J. 2003, Geophys. Res. Lett., 30, 30
Zhang, X., West, R. A., Banfield, D., & Yung, Y. L. 2013, Icarus, 226, 159
Zhang, X., West, R. A., Irwin, P. G. J., Nixon, C. A., & Yung, Y. L. 2015, Nat. Commun., 6, 1

Appendix A: C_6H_6 column density

The column density for C_6H_6 was calculated assuming a mean gravity of 26.1 m s^{-2}, a mean molar mass of 2.35 g mol^{-1} and the VMRs retrieved for models A, B and C with localized maximums at 5, 0.5 and 0.05 mbar, respectively. Fig. A.1 shows the column density map for both cases.

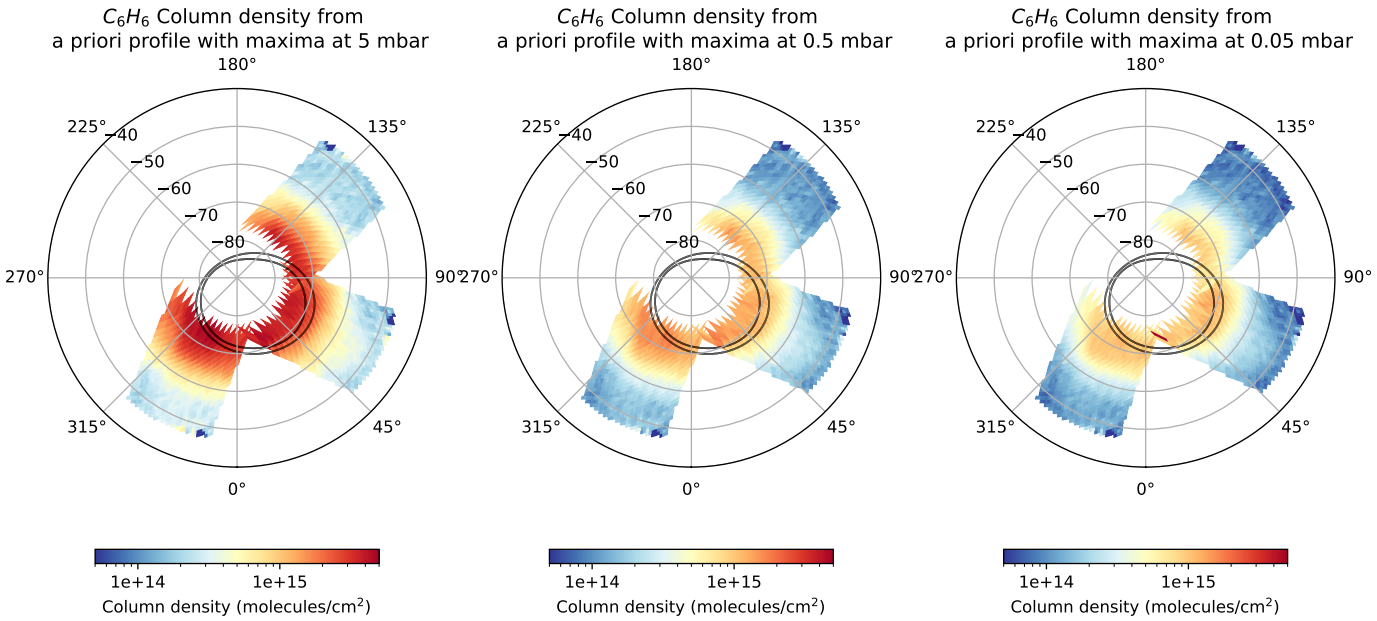

Fig. A.1. Column densities derived when using the three a priori profiles shown in section 3.1.

Appendix B: Goodness of the spectral fit

Fig. B.1 presents a comparison of the goodness-of-fit of a model with no haze, compared with the spectral fit of a model with the obtained haze profile.

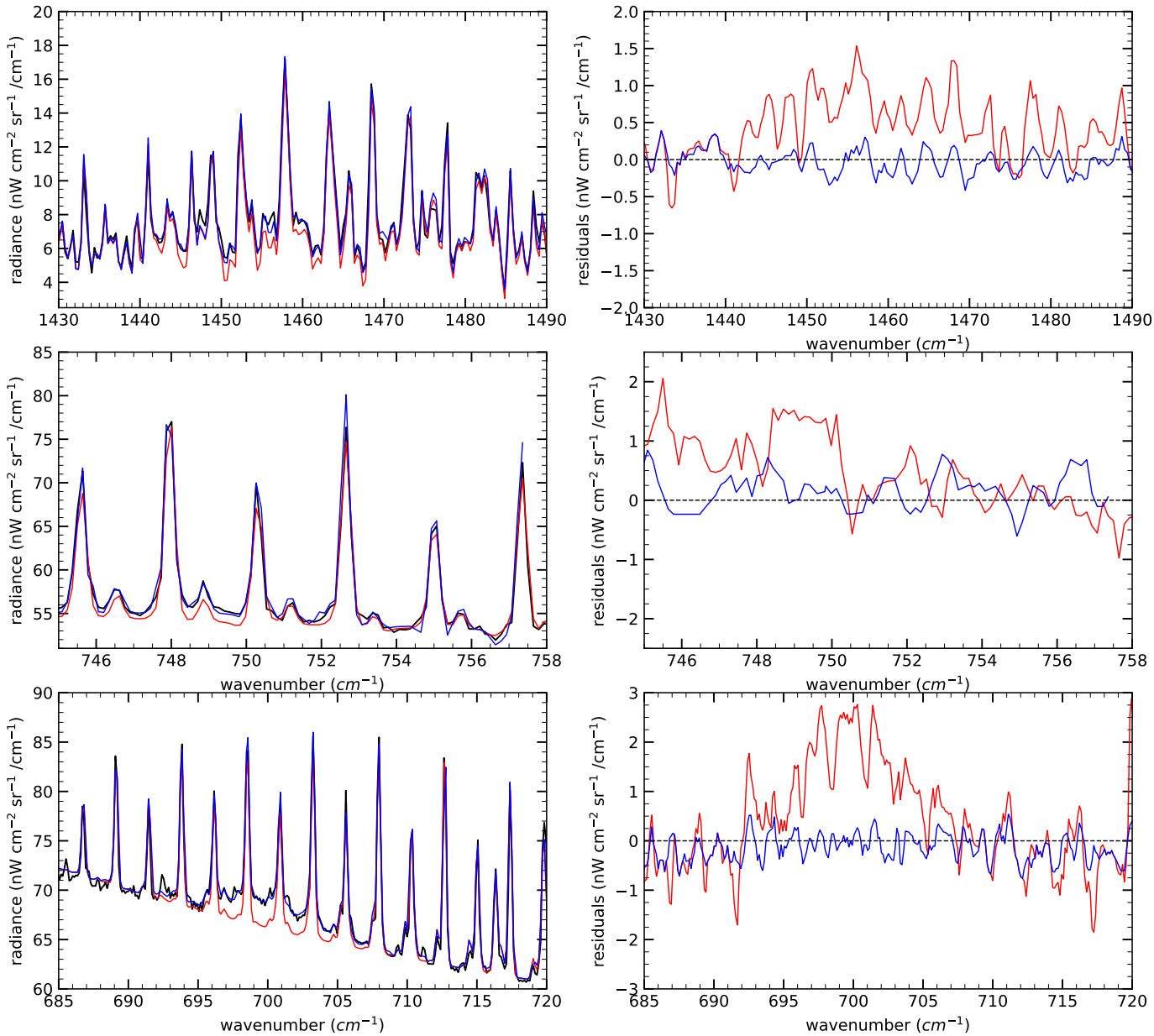

Fig. B.1. Left: MIRI/MRS latitudinal mean spectra acquired at 69°S (black) compared to the best fit of a spectrum without haze opacity (red) and the best fit of a spectrum with the opacity recovered in Fig. 11 (blue) for the ranges 1420 – 1480 (top), 685 – 720 (medium), and 743-760 (bottom) cm^{-1}. Right: Residuals between the models and the observed spectra for the spectral ranges analyzed.